PCCP

PAPER

View Article Online
View Journal

Cite this: DOI: 10.1039/d6cp00674d

Ab initio insights into plasmonic and strong-field contributions to H_2 dissociation on silver nanoshells

Natalia E. Koval, *[a] J. Iñaki Juaristi [bac] and Maite Alducin *[ac]

Modeling plasmonic catalysis by applying femtosecond laser pulses of high intensity (10^{13}–10^{15} W cm^{-2}), although justified by the time-dependent density functional theory (TDDFT) time-scale limitations, can lead to a dissociation mechanism that is completely unrelated to the plasmon excitation created under low-intensity continuous light in experiments (on the order of 1 W cm^{-2}). In this study, we examine the dissociation of H_2 on a large octahedral Ag nanoshell under varying field intensities, frequencies, and durations, and explore the possibility of identifying optimal modeling conditions accessible with current TDDFT simulations. We show that using this large nanoshell, which consists of an outer layer of the Ag_{231} cluster, it is still possible to disentangle the role of the plasmon from strong-field effects at applied field intensities as high as (2–8) $\times$ 10^{13} W cm^{-2}. In particular, although strong-field effects are always present at these intensities, we find that the excited plasmon dominates the dissociation process at the lowest applied intensity of 2 $\times$ 10^{13} W cm^{-2}. Furthermore, at the highest intensity, at which strong-field effects become dominant, the plasmon contributes to accelerating the dissociation of the molecule. Overall, our simulations pave the way for bridging the intensity gap between TDDFT modeling and experiments in plasmonic catalysis.

Received 24th February 2026,
Accepted 20th May 2026

DOI: 10.1039/d6cp00674d

rsc.li/pccp

1 Introduction

Plasmonic catalysis is a promising field of research that explores the use of localized surface plasmon resonance (LSPR) in metal nanoparticles to accelerate and enhance chemical reaction rates under the influence of light.[1–16] Experimentally, there are multiple studies showing that the rate of molecular dissociation at metal nanoparticle surfaces increases when the system is illuminated with a light of the same frequency as the plasmon resonance of the nanoparticle.[4,17–21] The effect is often explained by the plasmon decay that creates energetic charge carriers (“hot electrons”) in the nanoparticle that can transfer to the adsorbed molecule, leading to the weakening of its bonds.[17,18,21] For silver nanoparticles, a 4-fold[17] to 8-fold[22] acceleration of the chemical reaction was observed under resonant light illumination. However, the precise mechanism of the plasmon-induced molecular dissociation cannot be understood from experiments alone due to the short time of plasmon excitation and decay (on the order of femtoseconds, fs) that cannot be resolved experimentally. On top of that, the mechanism can be system-specific and is still a highly debated issue.[23–25] Therefore, *ab initio* calculations are crucial for getting insights into the interplay between plasmon excitation in a metal nanoparticle and dissociation of molecules adsorbed on its surface.

Time-dependent density functional theory (TDDFT)[26–28] combined with Ehrenfest dynamics (ED) is a state-of-the-art methodology that can describe electronic and atomic excitations at the nanoscale and on the femtosecond time scale.[29] Real-time TDDFT allows for an accurate (formally exact, but practically limited by the choice of the exchange–correlation functional) description of the plasmon excitation and decay. TDDFT-ED can be used to describe the atomic motion following the plasmon decay. Since ED is a mean-field approach, the dynamics follows a single average trajectory, so that it cannot account for different pathways associated with different electronic quantum states,[30] which may be relevant in the dissociation processes. However, TDDFT-ED is one of the very few methods capable of handling complex light–matter interactions and the electron and nuclear dynamics following a plasmon decay. Thus, despite its limitations, this approach can provide valuable insights into the mechanisms of plasmonic catalysis.

[a] *Centro de Física de Materiales CFM/MPC (CSIC-EHU), Paseo Manuel de Lardizabal 5, 20018 Donostia-San Sebastián, Spain. E-mail: natalia.koval@ehu.eus, maite.alducin@ehu.eus*
[b] *Departamento de Polímeros y Materiales Avanzados: Física, Química y Tecnología, Facultad de Química (EHU), Apartado 1072, 20080 Donostia-San Sebastián, Spain*
[c] *Donostia International Physics Center (DIPC), Paseo Manuel de Lardizabal 4, 20018 Donostia-San Sebastián, Spain*

There is an increasing number of studies using TDDFT-ED that report plasmon-assisted dissociation of molecules on plasmonic nanoparticles of different sizes and shapes.[31–45] Due to the high computational cost of such calculations, these studies, aimed to model plasmon-induced reactions, are commonly performed for small systems irradiated with high-intensity laser pulses (10^{13}–10^{15} W cm^{-2}). These conditions accelerate the dissociation process, but can bring about strong-field effects[46] that are rarely discussed. Such a discrepancy in intensities makes it difficult to extrapolate *ab initio* results to experimental conditions (intensities of the order of 1 W cm^{-2}) because strong-field effects can suppress the role of plasmon excitation and change the mechanism of molecular dissociation, as demonstrated recently in small ($\approx$1 nm) nanoparticles.[47] In that work,[47] we studied H_2 dissociation on a silver nanoshell (a hollow shell consisting of the outer layer of the icosahedral Ag_{55}) and compared the results obtained when applying both resonant and off-resonant (with the nanoparticle plasmon frequency) external fields of high intensities. Our TDDFT-ED calculations showed that both the metal nanoshell and H_2 become ionized at these high intensities because of multiphoton absorption. As a result, H_2 dissociates at both resonant and off-resonant pulse frequencies, making it difficult to determine the contribution of plasmon excitation to the process.

Motivated by the findings that emphasized the need to reconsider the use of strong external fields in plasmonic catalysis simulations, the aim of this work is twofold. First, we assess the possibility of reducing nonlinear effects while using external field intensities that allow us to access the reaction timescale with current TDDFT-ED simulations. Second, we conduct a thorough analysis of the dissociation mechanism to identify the role of plasmon and its interplay with strong-field nonlinear effects.

One possible way of reducing strong-field effects without reducing the intensity of the external pulse is to use large nanoparticles. It has been shown that the threshold intensity for dissociation decreases with increasing nanoparticle size.[48] Therefore, by modeling larger systems, it is possible to determine the optimal external field conditions that would generate strong plasmonic excitation, while reducing nonlinear effects without significantly increasing the dissociation timescale. In particular, we present a comprehensive analysis of the plasmon effect on an H_2 molecule adsorbed at the vertex of an octahedral silver nanoshell[49] under various external field conditions. The choice of the octahedron is motivated by the stronger field enhancement that the plasmon creates on its vertex compared to other shapes.[50–53] This property can additionally increase the effect on the molecule at a lower external field intensity. By comparing different field durations, frequencies (resonant *vs.* off-resonant), and peak intensities, we analyze the correlation between plasmonic and strong-field effects in detail.

2 Computational methodology

2.1 Geometry optimization

The first step in our computational approach involves optimization of the system's geometry using density functional theory (DFT). We used the Perdew–Burke–Ernzerhof (PBE) functional[54] within the CP2K software package,[55–57] which implements the Gaussian plane wave (GPW) method.[58,59] We used DZVP basis sets including 1 and 11 electrons for H and Ag, respectively, and a cutoff of 600 Ry for the plane wave auxiliary basis set. Norm-conserving Goedecker–Teter–Hutter (GTH) pseudopotentials[60] were used to represent the interaction of valence electrons with atomic cores. The initial coordinates of the octahedral Ag_{231} cluster (edge length 7 atoms) were obtained using the Atomic Simulation Environment (ASE) builder (function ase.cluster.Octahedron).[61] The nanoshell (denoted hereafter Ag_{231}^{L1}) was next constructed by taking only the outer layer of the unrelaxed Ag_{231} cluster, which is formed by 146 atoms. The H_2 molecule was placed at one nanoshell vertex with its molecular axis oriented parallel to the octahedron base (see Fig. 1a). The *z*-axis is defined along the inner diagonal that contains the vertex at which H_2 adsorbs. Note that the nanoshell with an inner diagonal of 2.45 nm before relaxation is smaller than those commonly employed in experiments. However, although less often, nanoparticles as small as a few nanometers have been studied experimentally as well.[62,63]

Using a non-periodic simulation cell of 32 × 32 × 32 Å^3, the Ag_{231}^{L1} + H_2 geometry was optimized until all atomic forces were below 0.001 Ha Bohr^{-1}. After relaxation, the edges of the nanoshell (colored in green in Fig. 1a) slightly bent towards the inner empty space of the hollow shell, whereas the facets (blue atoms in Fig. 1a) bent slightly outwards. The adsorption of H_2 causes a slight distortion of the nearest Ag atoms, with the underneath Ag vertex being displaced towards H_2. The optimized distance between the Ag vertex and the H_2 center of mass (CM) is 2.275 Å. The adsorbed H_2 remains parallel to the octahedron base with an equilibrium bond length of 0.763 Å. The adsorption energy E_{ads} = −0.17 eV is calculated from the ground state DFT + PBE energies using the formula $E_{ads} = E_{Ag_{231}^{L1}+H_2} - E_{Ag_{231}^{L1}} - E_{H_2}$. Similarly, the Ag_{231}^{L1} + H_2 ionization potential I_p = 4.6 eV is obtained as the ground state energy difference between the positively charged and neutral systems, *i.e.*, $I_p = E_{(Ag_{231}^{L1}+H_2)^+} - E_{(Ag_{231}^{L1}+H_2)^0}$.

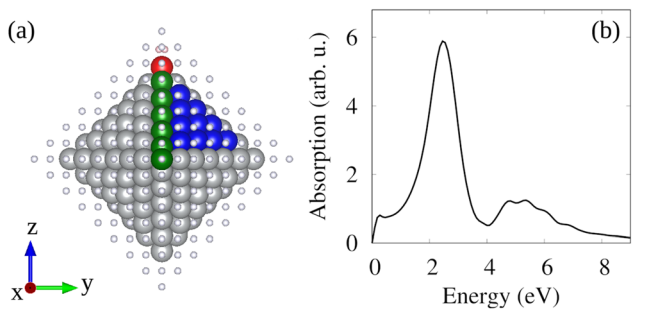

Fig. 1 (a) Relaxed structure of the Ag_{231}^{L1} nanoshell with H_2 (light pink spheres) adsorbed at 2.275 Å from the vertex (red sphere) surrounded by a layer of 258 ghost Ag atoms (small gray spheres). To facilitate visualization, green and blue spheres depict the nanoshell edge and facet Ag atoms, respectively. (b) Absorption spectrum of Ag_{231}^{L1} + H_2 calculated with RT-TDDFT, showing the plasmon resonance at $\hbar\omega_p$ = 2.48 eV.

2.2 Real-time time-dependent density functional theory calculations of the absorption spectrum

The $Ag_{231}^{L1} + H_2$ absorption spectrum was calculated within the real-time time-dependent density functional theory (RT-TDDFT) approach implemented in the CP2K software package[55–59,64,65] by perturbing the system with a weak broadband electric field, $E(t) = E_0\delta(t)\hat{\mathbf{e}}$.[66] In particular, we applied a z-polarized δ-kick field of strength $E_0 = 0.001$ a.u. ≈ 0.5 V nm^{-1} at $t = 0$ and let the system orbitals evolve in time during 25 fs using the enforced time reversible symmetry (ETRS) real-time propagation scheme with a time step $\Delta t = 0.005$ fs. Calculations were performed in the same non-periodic cell of $32 \times 32 \times 32$ Å^3 as that employed for geometry optimization. The absorption spectrum in the frequency domain was next computed by applying a discrete Fourier transform to the (induced) time-dependent dipole moment. For completeness, we also calculated the optical absorption spectra for x- and y-polarized electric fields and found them almost identical because of the symmetry of the nanoshell. The absorption spectrum for the z-polarized field is shown in Fig. 1b. It features an intense and well-defined plasmon peak at $\hbar\omega_p = 2.48$ eV and a less intense signal that extends from 4 to 7 eV, approximately. A similar optical absorption spectrum was obtained with RT-TDDFTB for the closely related system $Ag_{231} + H_2$, showing the plasmon peak at around 2.9 eV and a high-energy broad signal above 3 eV that is attributed to d-sp intraband transitions.[48] Experimentally, localized-surface plasmon resonances of 2.75–3.0 eV were measured in synthesized Ag octahedra with edge lengths varying in the range of 20–70 nm.[67]

2.3 Ehrenfest molecular dynamics simulations

The response of the electrons and nuclei to an external field was studied with the real-time TDDFT simulations combined with Ehrenfest molecular dynamics (ED) as implemented in the CP2K software package.[55–59,64,65] The external field was modeled by a Gaussian envelope:

$$\mathbf{E}(\omega, t) = E_0 \exp\left[-\frac{(t-t_0)^2}{2\sigma^2}\right] \cos[\omega(t-t_0)]\hat{\mathbf{k}}, \qquad (1)$$

where σ is the standard deviation and t_0 is the center of the envelope. The electric field was polarized in the z-direction. The maximum intensity is given by $I_{max} = c\varepsilon_0 {E_0}^2$, where c is the speed of light, ε_0 is the permittivity in vacuum, and E_0 is the maximum field strength. In order to determine those field conditions that allow us to distinguish between plasmon and strong-field contributions when studying the catalytic properties of plasmonic nanoparticles, we have applied four different pulses, resonant ($\hbar\omega = \hbar\omega_p = 2.48$ eV) and off-resonant ($\hbar\omega = 8$ eV), of varying intensities and durations to the $Ag_{231}^{L1} + H_2$ system. The intensity and duration of each pulse are summarized in Table 1 and depicted in Fig. S1. We note that the spectral width of the shortest pulse-4 at 2.48 eV is contained within the plasmon resonance peak, such that the excitation remains dominated by the collective plasmon mode and contributions from off-resonant electronic excitations are expected to be negligible. On the other hand, at 8 eV, there is no spectral overlap with any resonance (Fig. S2).

Table 1 Gaussian pulses applied to $Ag_{231}^{L1} + H_2$ in TDDFT-ED

	pulse-1	pulse-2	pulse-3	pulse-4
I_{max} (W cm^{-2})	2×10^{13}	2×10^{13}	2×10^{13}	8×10^{13}
t_0 (fs)	18	35	55	9
σ (fs)	5	10	15	2.5

For each applied field, the TDDFT-ED simulations were initiated from the optimized geometry of the H_2 molecule adsorbed on the nanoshell, while the initial atomic velocities correspond to an initial temperature of 300 K. All atoms were allowed to move freely without any geometry constraints during the dynamics (*i.e.*, no frozen atoms). We used a converged time step $\Delta t = 0.002$ fs and a non-periodic unit cell of size $40 \times 40 \times 45$ Å^3. Since CP2K is based on atom-centered basis sets, this large cell allows us to account for possible electron emission by adding a layer of ghost atoms around the nanoshell, as done in ref. 47. In the present work, the ghost layer corresponds to the outer layer of an octahedral nanocluster with an edge length of 9 atoms (see Fig. 1a, the coordinates are listed in the SI). The ghost atoms Ag_g are represented by the Ag DZVP basis set and the GTH pseudopotentials.

Data analysis and visualization were performed using NumPy,[68] Matplotlib,[69] VESTA,[70] and Gnuplot.[71]

3 Results and discussion

At an external field frequency matching the plasmon resonance, the metal nanoparticle exhibits a distinct, strong response in the linear regime. The amplitude of the dipole moment induced in the system is much larger at the plasmon frequency than at any other frequency. In a strong field, a clear manifestation of the nonlinearity of the perturbation is the absence of such a resonant behavior. This is what we found for a small icosahedral nanoshell of the Ag_{55} cluster (Ag_{55}^{L1}),[47] as mentioned in the Introduction. At the usual intense fields employed in TDDFT-ED studies ($I_{max} \geq 10^{13}$ W cm^{-2}), there was no difference in the amplitude of the time-dependent dipole moments that were induced by fields in resonance or off-resonance with the Ag_{55}^{L1} plasmon mode. Therefore, our first step has been to assess whether field intensities in the order of 10^{13} W cm^{-2} fall within the linear response regime for the larger octahedral nanoshell studied here. In particular, we start by applying the Gaussian pulse, denoted as pulse-1 in Table 1, to the Ag_{231}^{L1} nanoshell with the H_2 adsorbate. Note that, under the same pulse excitation, the plasmon effects were completely masked in $Ag_{55}^{L1} + H_2$.[47]

The induced dipole moments for resonant and off-resonant external field frequencies are compared in Fig. 2a. The dipole moment at a plasmon frequency of 2.48 eV has a significantly larger amplitude than at a higher, off-resonant frequency of 8 eV (see the absorption spectrum in Fig. 1b). However, in the linear-response regime, the created plasmonic oscillations of the dipole moment persist long after the pulse is off (see the

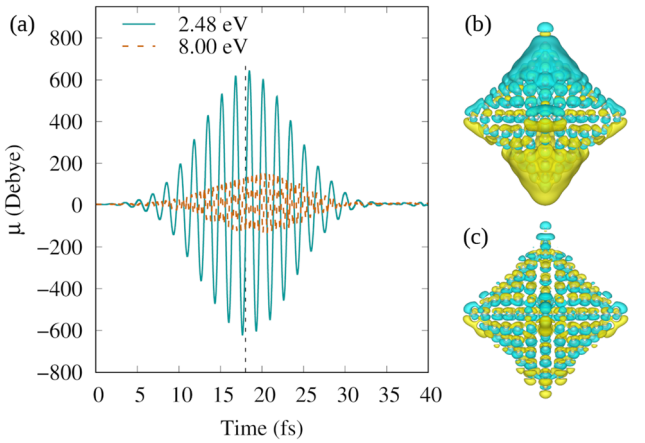

Fig. 2 (a) Transient dipole moment $\mu(t)$ of the Ag_{231}^{L1} + H_2 system induced by the Gaussian external field denoted pulse-1 in Table 1 with frequencies of 2.48 eV (resonant, cyan solid line) and 8 eV (off-resonant, orange dashed line). Vertical dashed line marks the time point t_0 = 18 fs of the pulse maximum. Corresponding Ag_{231}^{L1} + H_2 induced density created at time t = 10 fs (*i.e.*, near the induced dipole moment local maxima) by (b) the resonant pulse-1 (an isosurface value 0.00027588 e^- $Bohr^{-3}$) and (c) the off-resonant pulse-1 (an isosurface value 0.000148458 e^- $Bohr^{-3}$).

evolution of the dipole moment for a much lower intensity in Fig. S3).[72,73] Hence, the rapid decay of the dipole moment shown in Fig. 2a, which becomes almost zero immediately after the pulse is off, still manifests the nonlinear response of the system and it indicates that the applied perturbation is still strong. In spite of this, the analysis of the density changes induced by pulse-1 at the resonant frequency allows us to identify the distinct collective nature of the plasmon excitation, confirming that the plasmon is not suppressed. Fig. 2b and c show selected snapshots of the induced density created when applying the resonant and off-resonant pulse-1 to the Ag_{231}^{L1}-H_2 system. Each snapshot corresponds to the time point at which the value of the induced dipole (Fig. 2a) is close to one of its local maxima. When pulse-1 is resonant with $\hbar\omega_p$, we clearly observe the collective electron displacement that is characteristic of plasmon excitation (Fig. 2b). In contrast, when the pulse frequency is far from the resonance, at 8 eV, the distribution of the induced density suggests that only single- and multi-pair excitations are created (Fig. 2c). Altogether, the observed stronger dipolar response and corresponding induced density distribution under the resonant pulse-1 suggest that by applying an intense external field to the large nanoshell Ag_{231}^{L1}, we can keep the conditions closer to the linear regime, with a potential for distinguishing the role of plasmon in catalysis, as we analyze next.

In order to determine the plasmon contribution to the dynamics and possible dissociation of H_2 on Ag_{231}^{L1}, we have performed TDDFT-ED calculations by applying pulse-1 (Table 1) with frequencies $\hbar\omega$ = 2.48 eV (resonant) and 8 eV (off-resonant). Fig. 3a shows the time evolution of the H–H bond length for the two field frequencies. For comparison, it also includes the result for H_2 without the nanoshell (14 ghost atoms surround the molecule), in which case the molecule oscillates around its equilibrium bond length. When the

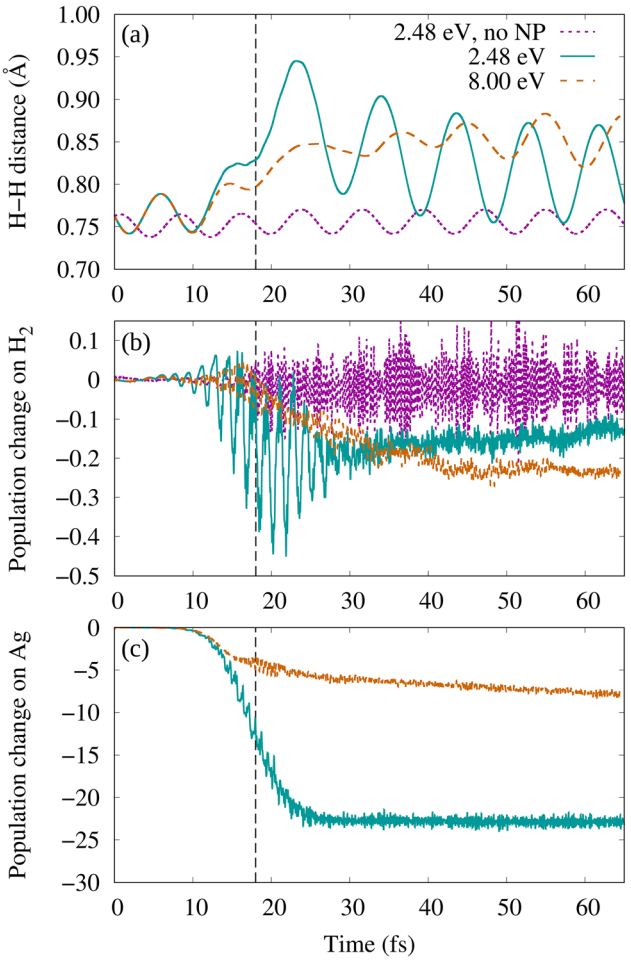

Fig. 3 (a) H_2 bond length and (b) and (c) Mulliken population change [$\Delta N_e = N_e(t) - N_e(t = 0)$] on H_2 and Ag_{231}^{L1}, respectively, as a function of time. Results obtained from TDDFT-ED simulations of H_2 adsorbed on Ag_{231}^{L1} using external field pulse-1 (see Table 1) at resonant (2.48 eV, cyan solid lines) and off-resonant (8 eV, orange dashed lines) frequencies. For comparison, the results obtained for a gas-phase H_2 when applying the resonant pulse-1 are also shown by magenta dotted lines in (a) and (b). Vertical dashed line marks the time point t_0 = 18 fs of the pulse maximum.

molecule is adsorbed on the nanoshell, the H–H bond is visibly stretched at both field frequencies during the interval around 10–30 fs (*i.e.*, while the pulse is more active), but the resonant pulse at $\hbar\omega$ = 2.48 eV produces the largest elongation. Once the pulse is extinguished, the molecule remains oscillating profoundly around a bond length of 0.8 Å in the case of the resonant pulse and around 0.85 Å, but with little variations, in the off-resonant case. Importantly, the molecule desorbs in both cases but without dissociating.

The observed changes in the H_2 bond length are associated with the changes in the electron population. Fig. 3 shows the transient electron population change [$\Delta N_e = N_e(t) - N_e(t = 0)$] experienced by the molecule (panel b) and the nanoshell (panel c). In each case, N_e is the number of electrons (not the charge) obtained from a Mulliken population analysis, with negative values of ΔN_e indicating a reduction in the number of electrons. Mulliken population analysis is employed as it

enables electron charge evaluation on ghost basis functions, while real-space partitioning schemes such as Hirshfeld and Bader do not provide a meaningful decomposition in the absence of atomic reference densities or regions of electron density minima between real and ghost atoms. Excitation of the plasmon mode in the case of the resonant pulse (2.48 eV), which is characterized by an oscillatory displacement of electrons between the adsorbate and the nanoshell, is reflected in the large-amplitude oscillations of ΔN_e that take place in the molecule while the pulse is on. Together with these oscillations, there is an underlying minor decrease of up to 0.1–0.2 electrons that persists once the external electric field is off. Inspection of the system orbitals remarks that many of them involve both the molecule and the nanoshell, as illustrated in Fig. S4. Therefore, this small ionization of the molecule is possibly related to the ionization of the nanoshell that loses more than 20 electrons according to the Mulliken analysis of the electron population change (Fig. 3c, cyan solid curve). Importantly, since the resonant frequency is smaller than the ionization potential of the system (4.6 eV), the existence of electron emission is a fingerprint of the strong-field effects associated with the intense pulse-1.

The absence of plasmon excitation in the case of the off-resonant pulse ($\hbar\omega$ = 8 eV) leads to much smaller oscillations of ΔN_e in the molecule (see orange dashed curve in Fig. 3b) and to minimal ionization of the nanoshell despite the fact that 8 eV is larger than the ionization potential and both single-photon and multi-photon absorption are possible (see orange dashed curve in Fig. 3c). As a result, the initial perturbation (10–30 fs) created by pulse-1 in the H–H bond is weaker in the off-resonant case, as shown in Fig. 3a. Notably, the isolated molecule does not lose any charge, supporting the fact that the electron population change on H_2 is mediated by the nanoshell. Altogether, the comparison of the results obtained with both field frequencies allows us to distinguish the plasmon from strong-field contributions. The large electron density fluctuations associated with the plasmon are responsible for a larger vibrational excitation of the molecule (larger oscillations of the H–H bond length). Furthermore, even though the plasmon energy is smaller than the system ionization potential and the off-resonant frequency, the excited plasmon also contributes to a higher ionization of the nanoshell by enhancing the coupling to the strong external field.

The observed rapid increase of the H–H bond length, occurring when the resonant pulse-1 is more intense (18 ± 5 fs), suggests that the duration of both the pulse and the excited plasmon, which decays rapidly once the pulse is off (Fig. 2a), was too short to cause dissociation. Therefore, to assess the effect of a longer perturbation, we have performed TDDFT-ED simulations for two additional resonant pulses, pulse-2 (Fig. S1b) and pulse-3 (Fig. S1c) in Table 1, that share I_{max} but have durations two and three times longer, respectively, than that of pulse-1.

Fig. 4a shows the H–H bond length as a function of time for the three pulses. Contrary to the case of the shortest pulse-1, both pulse-2 and pulse-3 induce molecular dissociation and desorption of the nascent H atoms. An H–H distance of 3.5 Å that is achieved with the two pulses during the time span of the simulations assures that H_2 is dissociated (see the potential energy as a function of the internuclear distance for isolated and adsorbed H_2 in Fig. S5). The electron population changes in Fig. 4b show that the longer durations of pulse-2 and pulse-3 facilitate the ionization of the molecule, which subsequently dissociates. In both cases, we recognize the large-amplitude oscillations in ΔN_e that are associated with plasmon excitation and the underlying decrease in the electron population that was observed with pulse-1. The difference is the higher degree of H_2 ionization that is reached because the new pulses are longer. As noted previously, H_2 ionization is linked to the ionization of the nanoshell that loses 35 (pulse-2) and 45 (pulse-3) electrons (see Fig. S6).

In the previous analysis (Fig. 4), not only is the duration of the pulses different but also their total energy. Therefore, the obtained H_2 dissociation can simply be a consequence of increasing the pulse energy when the maximum intensity is kept constant. In the following, we compare the H_2 dynamics on the Ag^{L1}_{231} nanoshell induced by pulses with the same total energy, but different maximum intensities and durations. In particular, we have performed TDDFT-ED simulations for both resonant and off-resonant field frequencies using pulse-4, which is four times shorter than pulse-2 and has a four times higher maximum intensity (I_{max} = 8 × 10^{13} W cm^{-2}) than the previous pulses (see Table 1 and Fig. S1d). Despite its high intensity, the plasmon excitation created by pulse-4 is still visible. This can be seen from the larger transient dipole

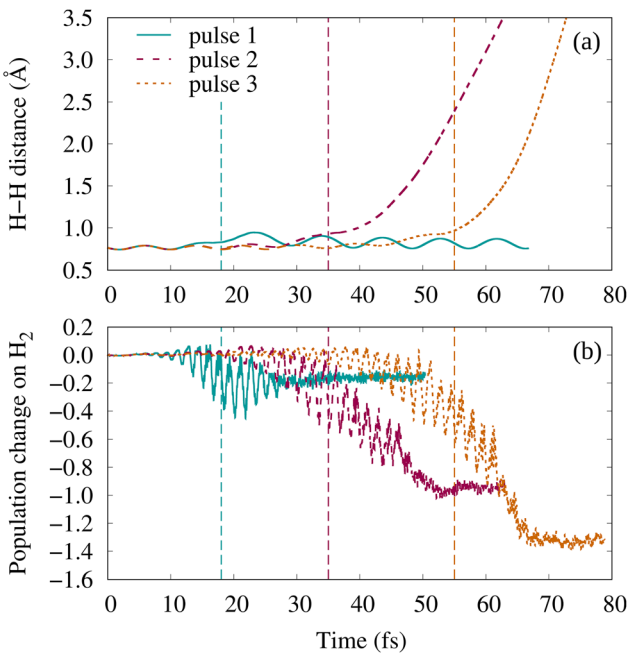

Fig. 4 (a) Time evolution of the H–H internuclear distance and (b) Mulliken population change [$\Delta N_e = N_e(t) - N_e(t = 0)$] on H_2. Results obtained from TDDFT-ED simulations for Ag^{L1}_{231} + H_2 using pulse-1 (cyan solid line), pulse-2 (magenta dashed line), and pulse-3 (orange dotted line) as resonant (2.48 eV) external fields (see Table 1 for pulse details). Peak intensity time points t_0 are marked by vertical dashed lines following the same color code.

moment amplitude induced by pulse-4 at the resonant frequency compared to the off-resonant frequency (see Fig. S7).

The time evolution of the H–H internuclear distance under pulse-2 and pulse-4 is compared in Fig. 5a. Both pulses induce H_2 dissociation at the resonance frequency, but the shorter and more intense pulse-4 also does so under off-resonant conditions. Therefore, pulse-2 provides the most explicit demonstration of plasmon effects, as the excitation of the plasmon is key to inducing H_2 dissociation. However, it should be noted that pulse-4 causes the molecule to dissociate much faster at the resonance frequency, demonstrating the importance of the plasmon effect even for this intense pulse. It is worth noting that the molecule ultimately desorbs regardless of whether it dissociates or not (see Fig. S8). Although direct comparison to experiments is still questionable due to differences in field intensity and timescale between *ab initio* simulations and experiments, our results are consistent with the observed acceleration of chemical reactions under resonant light.[22]

The results regarding the evolution of the H–H bond are consonant with the strength and nature of the H_2 ionization induced by each pulse and field frequency. This is observed in Fig. 5b, in which we show the Mulliken population change on H_2. As found previously with pulse-1, the plasmon excitation is demonstrated by the large-amplitude charge oscillations that are obtained for both pulses at 2.48 eV, but not at the high off-resonant frequency of 8 eV. Remarkably, the degree of ionization of the molecule (around one electron), which is inherently a strong-field effect, is also larger with the resonant pulses. The same is observed when comparing the electron population change on the nanoshell (Fig. S9). This is a clear indication that the excitation of the plasmon facilitates the electron emission that, ultimately, causes the dissociation of the molecule. Strong-field plasmonic (multiphoton) photoemission from silver nanoparticles has also been observed experimentally under similar laser intensities (10^{12}–10^{14} W cm^{-2}) due to a stronger field enhancement at LSPR.[74,75]

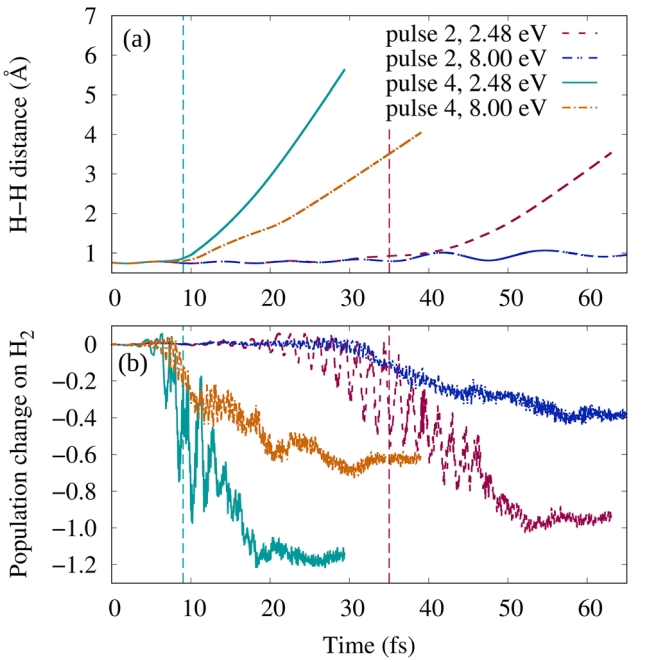

Fig. 5 (a) H–H internuclear distance and (b) Mulliken population change [$\Delta N_e = Ne(t) - N_e(t = 0)$] on H_2 as a function of time for pulse-2 and pulse-4 (see pulse details in Table 1) at resonant (2.48 eV) and off-resonant (8 eV) field frequencies. The results were obtained from TDDFT-ED simulations for Ag^{L1}_{231} + H_2. Vertical cyan (pulse-4) and magenta (pulse-2) lines show the time points corresponding to the maximum of each pulse.

The fact that pulse-4 is more intense than pulse-2 is reflected in the larger H_2 ionization that occurs at the same field frequencies. As a consequence, at this field strength, the molecule also dissociates with the off-resonant pulse-4, despite the absence of plasmon excitation. In this case, although ionization amounts to just $\approx$0.6 electrons at the end of the dynamics, it is sufficient to induce dissociation of the molecule. The chemical reaction in this particular case is therefore a purely strong-field effect in which plasmon excitation does not play any role.

The comparative analysis of the induced electric field $\mathbf{E}_{ind}$ provides direct evidence of the different perturbations that each pulse creates in the Ag^{L1}_{231} + H_2 system and it can allow us to discern how the plasmon excitation, on the one hand, and the strong-field effects, on the other hand, contribute to the observed dissociation. Fig. 6 and 7 show selected snapshots of the strength of the induced electric field created by pulse-2 and pulse-4, respectively, at resonant (panels a and b) and off-resonant (panels c and d) frequencies. The induced field is computed from the induced electron density as explained in the SI. The two snapshots shown for each pulse and frequency correspond to the time point at which the modulus of the induced dipole moment is close to a local maximum (see Fig. S11 and S12) and oriented either parallel or opposite to the z-axis. Each snapshot shows the instantaneous (z, y)-distribution of the x-averaged modulus of the electric field induced on Ag^{L1}_{231} + H_2 by the external pulse, $\langle \|\mathbf{E}_{ind}(y, z; t)\| \rangle_x$. Starting with pulse-2, Fig. 6a and b show that excitation of the plasmon mode at the resonant frequency leads to a high induced field that oscillates in time between the two opposite vertices located along the z-direction, extending well outside the nanoshell. Most of the perturbation is thus transiently localized on the molecule, with the highest values varying in the range of 1.1–1.3 V Å^{-1} (see Fig. S14). In contrast, off-resonant pulse-2 creates a much weaker induced field that, in addition, is mostly localized on the nanoshell and not on the molecule, as shown in Fig. 6c and d. Thus, the observed dissociation at the resonant pulse-2 is a consequence of the plasmon-enhanced high induced electric field that is created on the molecule.

In the case of pulse-4, the induced electric field at both the resonant (Fig. 7a and b) and off-resonant (Fig. 7c and d) frequencies behaves similarly to that of pulse-2. The difference is that the induced electric field created by the more intense pulse-4 is also stronger. Thus, even if the regions where E_{ind} is more intense with the off-resonant pulse are localized at the nanoshell faces, the values at the vertex where the molecule is adsorbed are transiently high (0.9–1.0 V Å^{-1}, see Fig. S20) and comparable to those created by the resonant pulse-2. As a result, the molecule also dissociates with the off-resonant pulse-4. Altogether, the results obtained with pulse-2 and pulse-4

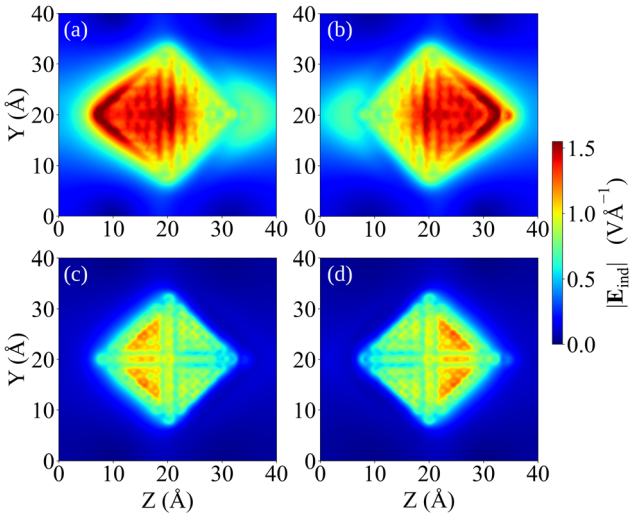

Fig. 6 (z, y)-distribution of the x-averaged electric field induced on Ag_{231}^{L1} + H_2 by the external pulse-2 at different time points t, $\langle \|\mathbf{E}_{ind}(y,z;t)\| \rangle_x$. Selected t correspond to time points at which the induced dipole moment $\mu_z(t)$ (see Fig. S11) is close to a local minimum (left panels) and maximum (right panels). (a) and (b) Snapshots for the resonant field frequency 2.48 eV at time points t = 34.25 and 35 fs, with the actual maximum induced electric field values of 1.53 and 1.65 V Å^{-1}, respectively. (c) and (d) Snapshots of the off-resonant field frequency 8 eV at time points t = 34 and 34.25 fs, with actual maximum values of 1.16 and 1.31 V Å^{-1}, respectively. The H_2 center of mass coordinates are approximately $Z \approx 34$ Å, $Y \approx 20$ Å.

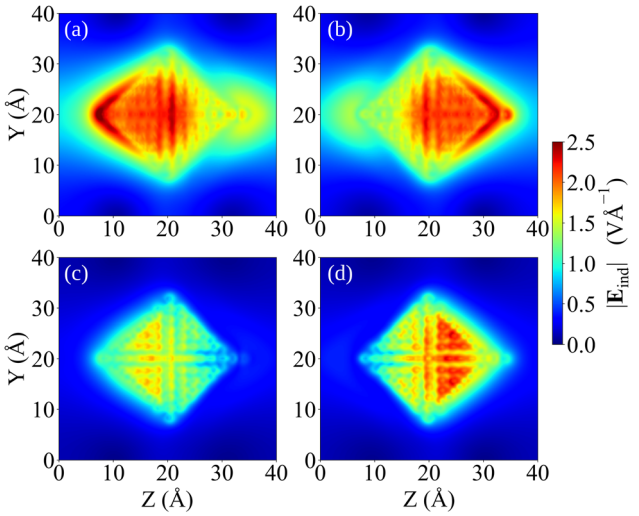

Fig. 7 Same as Fig. 6 but for pulse-4. (a) and (b) Snapshots for the resonant field frequency 2.48 eV at time points t = 9.24 and 10 fs (see Fig. S12), with actual maximum induced electric field values of 2.69 and 2.37 V Å^{-1}, respectively. (c) and (d) Snapshots for the off-resonant field frequency 8 eV at time points t = 9.24 and 10 fs, with actual maximum induced electric field values of 1.84 and 2.32 V Å^{-1}, respectively. The H_2 center of mass coordinates are approximately $Z \approx 34$ Å, $Y \approx 20$ Å.

remark that the amount of energy provided by the external field is not the only defining parameter, as it is utilized much less effectively in the off-resonant case. At resonance, plasmonic field enhancement concentrates the energy near the molecule, enabling efficient electron emission and bond dissociation. In contrast, off-resonant excitation results in a weaker effect on the molecule.

4 Conclusions and outlook

In summary, we have analyzed whether plasmonic effects can still be observed in photoinduced chemical reactions on nanoparticles when using the high-intensity laser pulses (10^{13}–10^{14} W cm^{-2}) required for TDDFT-ED simulations. In particular, we have focused on the dissociation of H_2 adsorbed on a plasmonic nanoparticle as a case study because dissociation is often one of the key elementary processes in heterogeneous catalysis at surfaces. Once the relevant reactants are dissociated, the subsequent reaction may proceed on the surface through conventional Langmuir–Hinshelwood or Eley–Rideal mechanisms, depending on whether all the reactants are adsorbed or involve reactions between adsorbates and gas-phase species.

Our simulations show that by increasing the size of the nanoparticle, we can indeed distinguish plasmonic effects that were completely suppressed by strong-field effects in the small nanoparticle studied in our previous work.[47] However, for the nanoparticle size and field intensities employed, nonlinear effects are manifested. The obtained dissociation of the H_2 molecule requires that it loses one electron. Moreover, it can take place even under off-resonant conditions when applying a short (2.5 fs) but very intense (8×10^{13} W cm^{-2}) external pulse. However, the effect of the plasmon can be clearly distinguished in all cases when comparing the response of the system under resonant and off-resonant pulses. The plasmon excitation generated by the former induces much larger charge oscillations on the molecule. The induced electric field is also stronger and is more localized on the molecule. As a result, depending on the intensity of the external field, the plasmon excitation can be decisive in provoking or accelerating the chemical reaction.

Actual experiments are performed in the linear regime with field intensities of the order of 1 W cm^{-2}, much lower than the ones used here. As discussed above, this means that nonlinear effects are still playing a role in these simulations. As a consequence, the extrapolation of the results to disentangle the mechanisms governing the experimental observations is still questionable. Nevertheless, the observation that, already at the utilized field intensities and nanoparticle sizes, the TDDFT-ED approach can account for plasmon induced photochemical processes constitutes a promising fact for future research. In this context, the present results provide practical guidelines for future TDDFT-ED studies. In particular, a systematic comparison between resonant and off-resonant excitation is a key diagnostic strategy to assess whether the plasmonic mechanism dominates. Moreover, our analysis indicates that increasing the nanoparticle size and extending the pulse duration at moderate intensity are more suitable than increasing peak intensity when aiming at preserving plasmon-driven dynamics while avoiding direct multiphoton ionization. The observed trends are expected to be true for other materials and

geometries, provided that a well-defined plasmon mode exists and that the adsorbate is located near the local field enhancement site. Following these criteria can help position simulations in a regime where the dynamics more closely resembles experimental conditions and facilitates a more direct connection between TDDFT-ED predictions and plasmonic catalysis experiments.

Author contributions

Conceptualization: NEK, MA, and JIJ; methodology: NEK and MA; calculations: NEK; data analysis and validation: NEK, MA, and JIJ; visualization: NEK; writing – original draft preparation: NEK; writing – review and editing: NEK, MA, and JIJ; funding acquisition: MA and JIJ. All authors have accepted responsibility for the entire content of this manuscript and have approved its submission.

Conflicts of interest

There are no conflicts to declare.

Data availability

The data generated during the current study are presented in the article and in the supplementary information (SI). Supplementary information: additional figures and theoretical details of the calculation of the induced fields. See DOI: https://doi.org/10.1039/d5cp00674d.

Acknowledgements

Financial support was provided by the Spanish MCIN/AEI/10.13039/501100011033/, FEDER Una manera de hacer Europa (Grant No. PID2022-140163NB-I00), Gobierno Vasco-EHU (Project No. IT1569-22), and the Basque Government Education Departments' IKUR program, also co-funded by the European NextGenerationEU action through the Spanish Plan de Recuperación, Transformación y Resiliencia (PRTR). The authors thankfully acknowledge the computer resources at MareNostrum and the technical support provided by the Barcelona Supercomputing Center (Projects No. RES-FI-2024-2-0022 and No. RES-FI-2025-1-0006) as well as the HPC resources provided by the Donostia International Physics Center (DIPC) Supercomputing Center.

References

1 S. Linic, P. Christopher and D. B. Ingram, *Nat. Mater.*, 2011, **10**, 911–921.
2 P. Christopher, H. Xin, A. Marimuthu and S. Linic, *Nat. Mater.*, 2012, **11**, 1044–1050.
3 S. Linic, U. Aslam, C. Boerigter and M. Morabito, *Nat. Mater.*, 2015, **14**, 567–576.
4 W. Hou and S. B. Cronin, *Adv. Funct. Mater.*, 2013, **23**, 1612–1619.
5 X. Zhang, Y. L. Chen, R.-S. Liu and D. P. Tsai, *Rep. Prog. Phys.*, 2013, **76**, 046401.
6 Q. Wei, S. Wu and Y. Sun, *Adv. Mater.*, 2018, **30**, 1802082.
7 Z. Zhang, C. Zhang, H. Zheng and H. Xu, *Acc. Chem. Res.*, 2019, **52**, 2506–2515.
8 E. Cortés, L. V. Besteiro, A. Alabastri, A. Baldi, G. Tagliabue, A. Demetriadou and P. Narang, *ACS Nano*, 2020, **14**, 16202–16219.
9 Y. Sivan and Y. Dubi, *Appl. Phys. Lett.*, 2020, **117**, 130501.
10 A. Kumar, P. Choudhary, A. Kumar, P. H. C. Camargo and V. Krishnan, *Small*, 2021, **18**, 2101638.
11 E.-R. Newmeyer, J. D. North and D. F. Swearer, *J. Appl. Phys.*, 2022, **132**, 230901.
12 V. Jain, R. K. Kashyap and P. P. Pillai, *Adv. Opt. Mater.*, 2022, **10**, 2200463.
13 M. J. Kale, T. Avanesian and P. Christopher, *ACS Catal.*, 2014, **4**, 116–128.
14 Y. Dong, C. Hu, H. Xiong, R. Long and Y. Xiong, *ACS Catal.*, 2023, **13**, 6730–6743.
15 A. Amirjani, N. B. Amlashi and Z. S. Ahmadiani, *ACS Appl. Nano Mater.*, 2023, **6**, 9085–9123.
16 C. Moularas, A. Gemenetzi, Y. Deligiannakis and M. Louloudi, *Nanoenergy Adv.*, 2024, **4**, 25–44.
17 P. Christopher, H. Xin and S. Linic, *Nat. Chem.*, 2011, **3**, 467–472.
18 S. Mukherjee, F. Libisch, N. Large, O. Neumann, L. V. Brown, J. Cheng, J. B. Lassiter, E. A. Carter, P. Nordlander and N. J. Halas, *Nano Lett.*, 2012, **13**, 240–247.
19 M. L. Brongersma, N. J. Halas and P. Nordlander, *Nat. Nanotechnol.*, 2015, **10**, 25–34.
20 C. Boerigter, R. Campana, M. Morabito and S. Linic, *Nat. Commun.*, 2016, **7**, 10545.
21 A. Cheruvathoor Poulose, G. Zoppellaro, I. Konidakis, E. Serpetzoglou, E. Stratakis, O. Tomanec, M. Beller, A. Bakandritsos and R. Zbořil, *Nat. Nanotechnol.*, 2022, **17**, 485–492.
22 B. Miralles, M. Y. Paredes, A. V. Bragas, G. Grinblat, E. Cortés and A. F. Scarpettini, *J. Phys. Chem. C*, 2024, **128**, 10017–10024.
23 C. L. Brosseau and E. Cortés, *Commun. Chem.*, 2024, **7**, 294.
24 R. Verma, G. Sharma and V. Polshettiwar, *Nat. Commun.*, 2024, **15**, 7974.
25 R. Miyar, I. W. Un, S. H. Lavan, Y. Dubi, J. H. Baraban, Y. Sivan and B. A. Rosen, *ACS Catal.*, 2025, **15**, 2359–2366.
26 E. Runge and E. K. U. Gross, *Phys. Rev. Lett.*, 1984, **52**, 997–1000.
27 M. A. L. Marques, *Time-Dependent Density Functional Theory*, Springer, Berlin Heidelberg, 2006.
28 C. A. Ullrich, *Time-dependent density-functional theory: concepts and applications*, OUP, Oxford, 2011.
29 C. J. Herring and M. M. Montemore, *ACS Nanosci. Au*, 2023, **3**, 269–279.
30 J. C. Tully, *Chem. Phys. Lett.*, 2023, **816**, 140396.
31 L. Yan, Z. Ding, P. Song, F. Wang and S. Meng, *Appl. Phys. Lett.*, 2015, **107**, 083102.

32 Y. Zhang, T. Nelson, S. Tretiak, H. Guo and G. C. Schatz, *ACS Nano*, 2018, **12**, 8415–8422.
33 O. A. Hull, D. B. Lingerfelt, X. Li and C. M. Aikens, *J. Phys. Chem. C*, 2020, **124**, 20834–20845.
34 Y. Zhang, D. Chen, W. Meng, Z. Xu, H. Guo, S. Li and S. Meng, *J. Phys. Chem. C*, 2021, **125**, 26348–26353.
35 J. Huang, *PCCP*, 2021, **23**, 25629–25636.
36 G. U. Kuda-Singappulige and C. M. Aikens, *J. Phys. Chem. A*, 2021, **125**, 9450–9458.
37 Y. Zhang, L. Yan, M. Guan, D. Chen, Z. Xu, H. Guo, S. Hu, S. Zhang, X. Liu, Z. Guo, S. Li and S. Meng, *Adv. Sci.*, 2021, **9**, 2102978.
38 C. J. Herring and M. M. Montemore, *Chem. Mater.*, 2023, **35**, 1586–1593.
39 T. E. Li and S. Hammes-Schiffer, *J. Am. Chem. Soc.*, 2023, **145**, 18210–18214.
40 Y. Wang and C. M. Aikens, *J. Phys. Chem. A*, 2023, **127**, 5609–5619.
41 Y. Wang and C. M. Aikens, *J. Phys. Chem. A*, 2024, **128**, 3784–3793.
42 C. J. Herring and M. M. Montemore, *ACS Nano*, 2025, **19**, 9860–9867.
43 P. K. Verma, S. K. Nayak, K. Bhardwaj and S. S. R. K. C. Yamijala, *J. Phys. Chem. Lett.*, 2025, **16**, 4536–4546.
44 M. Kar and G. C. Schatz, *J. Phys. Chem. C*, 2025, **129**, 1758–1768.
45 W. Zhang, Q. Xiao and J. Wen, *J. Phys. Chem. Lett.*, 2025, 6073–6080.
46 T. Fennel, K.-H. Meiwes-Broer, J. Tiggesbäumker, P.-G. Reinhard, P. M. Dinh and E. Suraud, *Rev. Mod. Phys.*, 2010, **82**, 1793–1842.
47 N. E. Koval, J. I. Juaristi and M. Alducin, *Chem. Sci.*, 2024, **15**, 18581–18591.
48 S. K. Giri and G. C. Schatz, *J. Phys. Chem. C*, 2023, **127**, 4115–4123.
49 F. Huang, G. Ma, J. Liu, J. Lin, X. Wang and L. Guo, *Small*, 2016, **12**, 5442–5448.
50 A. Agrawal, I. Kriegel and D. J. Milliron, *J. Phys. Chem. C*, 2015, **119**, 6227–6238.
51 C. W. Moon, S. Y. Lee, W. Sohn, D. M. Andoshe, D. H. Kim, K. Hong and H. W. Jang, *Part. Part. Syst. Charact.*, 2016, **34**, 1600340.
52 J. L. Montaño-Priede and U. Pal, *J. Phys. Chem. C*, 2019, **123**, 11833–11839.
53 Y. Kang, S. M. João, R. Lin, K. Liu, L. Zhu, J. Fu, W.-C. Cheong, S. Lee, K. Frank, B. Nickel, M. Liu, J. Lischner and E. Cortés, *Nat. Commun.*, 2024, **15**, 3923.
54 J. P. Perdew, K. Burke and M. Ernzerhof, *Phys. Rev. Lett.*, 1996, **77**, 3865–3868.
55 J. Hutter, M. Iannuzzi, F. Schiffmann and J. VandeVondele, *Wiley Interdiscip. Rev.: Comput. Mol. Sci.*, 2013, **4**, 15–25.
56 T. D. Kühne, M. Iannuzzi, M. Del Ben, V. V. Rybkin, P. Seewald, F. Stein, T. Laino, R. Z. Khaliullin, O. Schütt and F. Schiffmann, *et al.*, *J. Chem. Phys.*, 2020, **152**, 194103.
57 CP2K version 9.1, 2021, https://www.cp2k.org/.
58 G. Lippert, J. Hutter and M. Parinello, *Mol. Phys.*, 1997, **92**, 477–487.
59 J. VandeVondele, M. Krack, F. Mohamed, M. Parrinello, T. Chassaing and J. Hutter, *Comput. Phys. Commun.*, 2005, **167**, 103–128.
60 S. Goedecker, M. Teter and J. Hutter, *Phys. Rev. B*, 1996, **54**, 1703–1710.
61 A. Hjorth Larsen, J. Jørgen Mortensen, J. Blomqvist, I. E. Castelli, R. Christensen, M. Dułak, J. Friis, M. N. Groves, B. Hammer and C. Hargus, *et al.*, *J. Phys.: Condens. Matter*, 2017, **29**, 273002.
62 A. Campos, N. Troc, E. Cottancin, M. Pellarin, H.-C. Weissker, J. Lermé, M. Kociak and M. Hillenkamp, *Nat. Phys.*, 2018, **15**, 275–280.
63 T. Deka, A. Das, S. John and R. G. Nair, *Int. J. Hydrogen Energy*, 2024, **72**, 1169–1183.
64 T. Kunert and R. Schmidt, *EPJD*, 2003, **25**, 15–24.
65 S. Andermatt, J. Cha, F. Schiffmann and J. VandeVondele, *J. Chem. Theory Comput.*, 2016, **12**, 3214–3227.
66 K. Yabana and G. Bertsch, *Phys. Rev. B:Condens. Matter Mater. Phys.*, 1996, **54**, 4484.
67 Y. Wang, D. Wan, S. Xie, X. Xia, C. Z. Huang and Y. Xia, *ACS Nano*, 2013, **7**, 4586–4594.
68 C. R. Harris, K. J. Millman, S. J. van der Walt, R. Gommers, P. Virtanen, D. Cournapeau, E. Wieser, J. Taylor, S. Berg and N. J. Smith, *et al.*, *Nature*, 2020, **585**, 357–362.
69 J. D. Hunter, *Comput. Sci. Eng.*, 2007, **9**, 90–95.
70 K. Momma and F. Izumi, *J. Appl. Crystallogr.*, 2011, **44**, 1272–1276.
71 T. Williams, C. Kelley and many others, Gnuplot 5.4: an interactive plotting program, https://gnuplot.sourceforge.net/, 2024.
72 D. Nishizawa, R. Amano, T. Taketsugu and T. Iwasa, *J. Chem. Phys.*, 2024, **161**, 054309.
73 P. K. Verma, V. B. Kumar and V. Srinivasan, *Adv. Opt. Mater.*, 2025, **13**, 2402679.
74 F. Evers, C. Rakete, K. Watanabe, D. Menzel and H.-J. Freund, *Surf. Sci.*, 2005, **593**, 43–48.
75 M. R. Bionta, S. J. Weber, I. Blum, J. Mauchain, B. Chatel and B. Chalopin, *New J. Phys.*, 2016, **18**, 103010.